



Electrical and photoluminescence properties of $(\text{Bi}_{0.5-x/0.94}\text{Er}_{x/0.94}\text{Na}_{0.5})_{0.94}\text{Ba}_{0.06}\text{TiO}_3$ lead-free ceramics

Li-na Liu¹ · Xiao-ming Chen¹ · Rui-yi Jing¹ · Han-li Lian² · Wen-wen Wu¹ · Yan-ping Mou¹ · Peng Liu¹

Received: 5 December 2018 / Accepted: 25 January 2019 / Published online: 5 February 2019
© Springer Science+Business Media, LLC, part of Springer Nature 2019

Abstract

In this paper, electrical and photoluminescence properties of the $(\text{Bi}_{0.5-x/0.94}\text{Er}_{x/0.94}\text{Na}_{0.5})_{0.94}\text{Ba}_{0.06}\text{TiO}_3$ lead-free ceramics with $x \leq 0.02$ were investigated. All ceramics have pure perovskite phase. Lattice distortion induced by the doping of Er^{3+} was observed. The ceramics show average grain sizes around 0.6–1.0 μm . The doped ceramics exhibit decreased dielectric constant, which are still higher than 1200 at room temperature. Curie temperatures of the samples do not fluctuate dramatically with changing the doping amounts, which are around 250 °C. The piezoelectric constant d_{33} is closely related to the Er^{3+} content. Under an excitation of 487 nm, the ceramics exhibit visible luminescent emissions at 528 nm (green), 548 nm (green), and 670 nm (red).

1 Introduction

In recent years, ferroelectric perovskites have been widely used in many fields [1–3]. Due to regulations about environmental protection, studies on lead-free materials become very hot [4–6]. Bismuth sodium titanate (BNT), as one of most promising candidates, has high Curie temperature and good ferroelectric properties [7, 8]. But, high coercive field of BNT ceramics always induces low piezoelectric performance. As has been reported, the solid solution of $(\text{Na}_{0.5}\text{Bi}_{0.5}\text{Ba}_{0.06})\text{TiO}_3$ exhibits a tetragonal–rhombohedral morphotropic phase boundary (MPB) [7, 9], which facilitates improving piezoelectric performance of the ceramics [10–12]. With the development of modern apparatus, it is very important to realize multifunction in one material. For example, the materials possessing optical and electrical properties can be used in solid-state laser, LED, dynamic random access memory, and photoelectric integrator, etc [13]. For realizing versatility of BNT-based materials, one frequently-used method is to add trivalent elements

of lanthanide [14]. Herabut et al. reported that the doping of La^{3+} could improve dielectric, piezoelectric, and electromechanical properties of the BNT system [15]. Sum et al. found that the adding of Pr^{3+} improved ferroelectric properties and increased intensity of red emission [16]. Hu et al. reported that the Er^{3+} -doped BNT-based materials exhibit excellent optical and electrical properties [17]. Lau et al. observed that point defects have great influence on the photoluminescence properties of the Er^{3+} -doped BNT-based ceramics [18]. These results demonstrate that the elements of lanthanide are effective in affecting both electrical and optical performances. In this work, conventional solid-state reaction method was used to prepare $(\text{Bi}_{0.5-x/0.94}\text{Er}_{x/0.94}\text{Na}_{0.5})_{0.94}\text{Ba}_{0.06}\text{TiO}_3$ ceramics. Their electrical and photoluminescence properties were investigated.

2 Experimental procedure

$(\text{Bi}_{0.5-x/0.94}\text{Er}_{x/0.94}\text{Na}_{0.5})_{0.94}\text{Ba}_{0.06}\text{TiO}_3$ (abbreviated as BN6BT:xEr, where $x=0, 0.0025, 0.005, 0.0075, 0.01, \text{ and } 0.02$) ceramics were obtained by means of a solid-state sintering method. Dried Na_2CO_3 (99.8%), Bi_2O_3 (98.9%), BaCO_3 (99.0%), TiO_2 (98.0%), and Er_2O_3 (99.9%) powders were chosen as starting materials. For each composition, the oxides and carbonates were weighed according to the chemical formula after drying. The powders were calcined at 900 °C after ball-milling for 24 h. The powders were pulverized via adding 5 wt% polyvinyl alcohol. The pellets

✉ Xiao-ming Chen
xmchen@snnu.edu.cn

¹ School of Physics and Information Technology, Shaanxi Normal University, Xi'an 710119, People's Republic of China

² School of Science, Xi'an University of Posts and Telecommunications, Xi'an 710121, People's Republic of China

were pressed under 280 MPa. The diameter of the pellets is 10 mm and the thickness is approximate 1.3 mm. The binder in green pellets was burned out at 500 °C before sintering. The pellets were sintered at 1150 °C and dwelling time was 2 h. During sintering, the pellets were covered by the corresponding powders.

X-ray diffraction (XRD) data were collected via a D/Max2550 XRD meter (Rigaku Co) and crystallite structure was refined via the General Structure Analysis System (GSAS) software package [19–21]. For microstructural analysis, the ceramics were thoroughly polished, thermally etched and then characterized using a Nova Nano 450 scanning electron microscope (SEM, FEI). Average size of grains was estimated by using software Nano Measurer and more than 200 grains were used to calculate grain size distribution. Agilent E4980A LCR meter was used to measure dielectric properties. The samples were poled at 50 kV/cm for 20 min at room temperature and then placed for 24 h. The piezoelectric coefficient d_{33} were measured via by means of a ZJ-4A d_{33} meter. Ferroelectric behavior was characterized on a ferroelectric analyzer (Precision Premier II) at room temperature. Fluorescence spectrophotometer (FluoroMax-4, HORIBA, USA) was used to measure photoluminescence of the ceramics.

3 Results and discussion

The theoretical density (ρ_t) of the ceramics was determined from the lattice volume (Table 1). The relative density (ρ_r) was calculated based on the equation of $\rho_r = \rho_b / \rho_t \times 100\%$, where ρ_b is bulk density and was obtained by using Archimedes method. The dependences of ρ_b , ρ_t , and ρ_r as a function of x are shown in Fig. 1. The ρ_b values of the ceramics are higher than 5.8 g/cm³ and change slightly with increasing x . All samples show ρ_r values around 98%, implying these ceramics were well sintered. The SEM images of the samples are displayed in Fig. 2, which exhibit dense microstructures. The grain boundaries are distinguishable. The size distribution of grains is shown in the insets of Fig. 2. The average grain sizes (D) are around 0.6–1.0 μm .

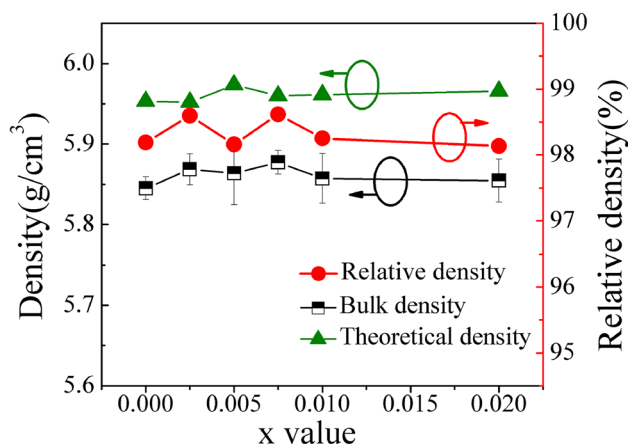


Fig. 1 The bulk density, theoretical density, and relative density of the ceramics

The XRD curves of the ceramics demonstrate that all ceramics were crystallized into single perovskite structure (Fig. 3a). Figure 3b presents the XRD peaks around 30°. The peak positions move toward right hand side, confirming the entrance of Er^{3+} into the lattice. It is well known that the composition of $(\text{Na}_{0.5}\text{Bi}_{0.5}\text{Ba}_{0.06})\text{TiO}_3$ exhibits a tetragonal–rhombohedral MPB [11, 26]. Crystallite structure of the ceramics was refined with a two-phase mixture model of R3c + P4bm and the results are shown in Table 1. As a typical example, the refinement result for the ceramics with $x = 0.0025$ is shown in Fig. 3c. The lattice parameters exhibit a decrease trend with the increase in Er^{3+} content, which can be attributed to the different radii between Bi^{3+} and Er^{3+} . Here, we want to mention that the radii of Bi^{3+} and Er^{3+} with coordination number (CN) of 12 are not available in Shannon's table [22]. The radius of Bi^{3+} with CN = 12 can be determined by extrapolation of the lower CN values [23], which is 1.36 Å, as reported in our previous work [24]. By means of the same method, the obtained radius of Er^{3+} with CN = 12 is below 1.23 Å. The smaller radius of Er^{3+} than that of Bi^{3+} causes the lattice shrinkage of the ceramics.

Figure 4a shows dielectric spectra of the unpoled samples. The dielectric loss ($\tan\delta$), dielectric constant (ϵ_r) at room temperature, maximum dielectric constant (ϵ_m), and

Table 1 Lattice parameters of the rhombohedral phase (a_{rh}) with the R3c space group ($Z = 1$) and those of the Tetragonal phase ($a_{\text{tr}}, c_{\text{tr}}$) with the P4bm space group ($Z = 2$)

Samples	a_{rh} (Å)	a_{tr} (Å)	c_{tr} (Å)	V_{rh} (Å ³)	V_{tr} (Å ³)
$x = 0$	3.9036(5)	5.5188(3)	3.9033(6)	59.4857(0)	59.4423(4)
$x = 0.0025$	3.9029(3)	5.5172(8)	3.9013(5)	59.4527(9)	59.3792(8)
$x = 0.005$	3.9008(1)	5.5172(0)	3.9027(1)	59.3559(6)	59.3982(6)
$x = 0.0075$	3.9000(4)	5.5176(8)	3.9014(7)	59.3208(2)	59.3897(2)
$x = 0.01$	3.8989(8)	5.5132(3)	3.9024(7)	59.2724(6)	59.3091(6)
$x = 0.02$	3.8955(1)	5.5104(8)	3.9017(5)	59.1143(5)	59.2390(7)

Lattice volumes of the rhombohedral phase (V_{rh}) and Tetragonal phase (V_{tr}) are also shown

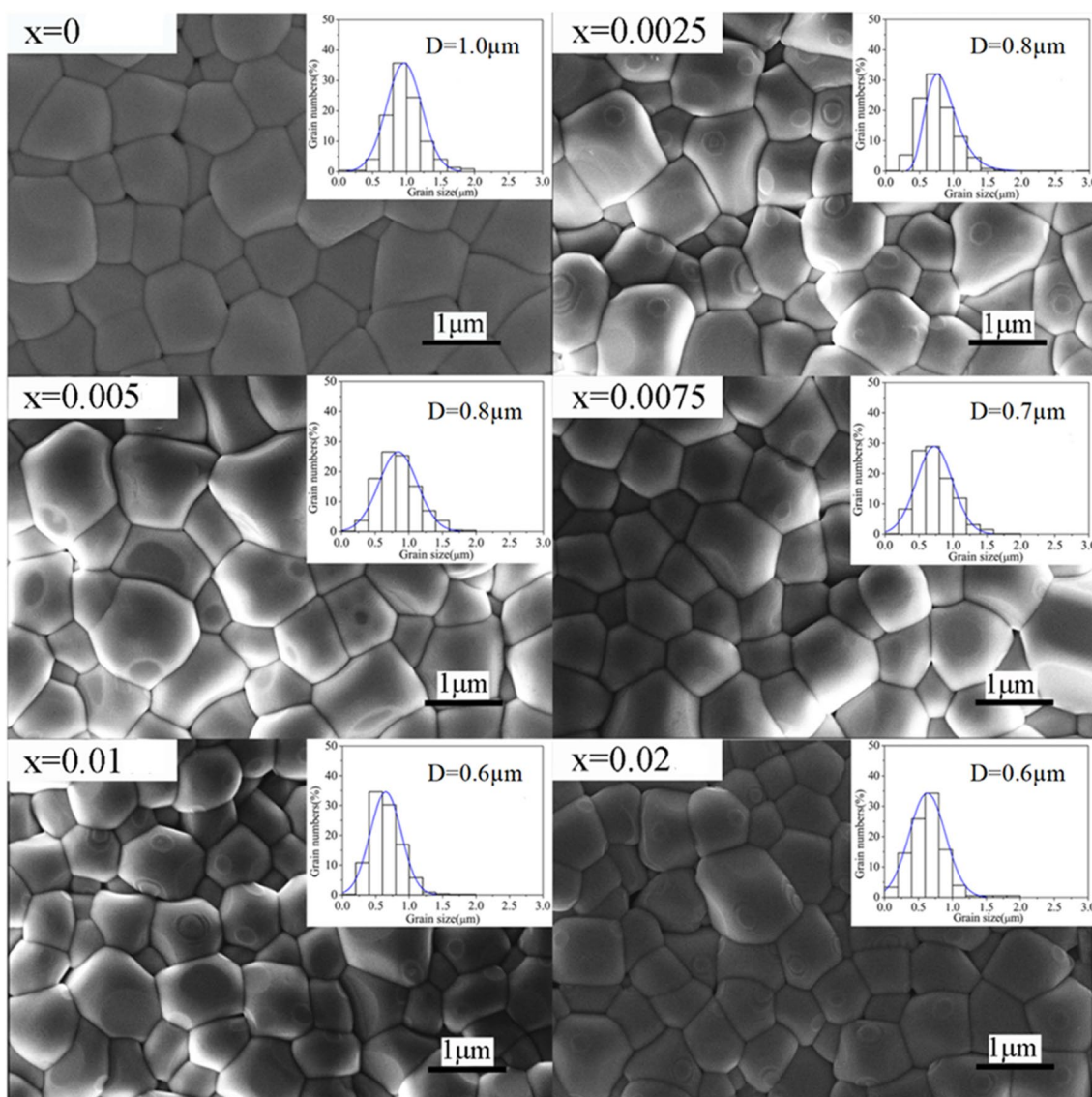


Fig. 2 SEM images of the ceramics. The insets show the distribution of grain size

Curie temperature (T_c) are exhibited in Table 2. Curie temperatures of the samples do not fluctuate dramatically with changing the doping amount, which are around 250 °C. The ceramic with $x = 0$ shows ϵ_r of 1853 at room temperature. The doped ceramics exhibit decreased ϵ_r values, which are still higher than 1200 at room temperature. The $\tan\delta$ values are around 0.04. The peaks of dielectric constant around T_c are obviously broadened, indicating diffuse character. The depolarization temperature (T_d) can be determined via the dielectric spectrum of the poled ceramics [24]. The changes of ϵ_r and $\tan\delta$ of the poled ceramics measured at 1 kHz as a function of temperature (T) are shown in Fig. 4b. The poled samples show a new dielectric anomaly on the $\epsilon_r \sim T$ curves at the temperature denoted as T_d . Correspondingly, a new peak appears on the

$\tan\delta \sim T$ curves. The obtained T_d values for the ceramics with $x = 0, 0.0025, 0.005, 0.0075, 0.01$ are 89 °C, 83 °C, 78 °C, 83 °C, and 78 °C, respectively. For the ceramic with $x = 0.02$, the dielectric anomaly was not observed. The Curie–Weiss (CW) law was used to explore diffuse behavior:

$$\frac{1}{\epsilon_r} = \frac{(T - T_0)}{C} \tag{1}$$

where C and T_0 are the CW constant and CW temperature, respectively [25]. As a typical example, the fitting result for the ceramic with $x = 0.0025$ via the CW law is shown in Fig. 4c. At temperature denoted as T_B , the ϵ_r value deviates from the fitting line. The obtained fitting values are

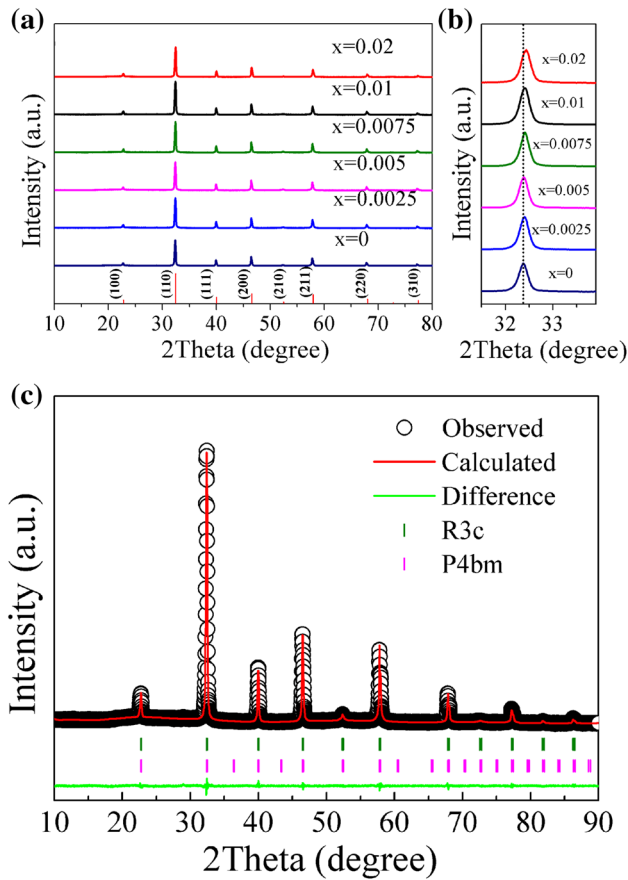
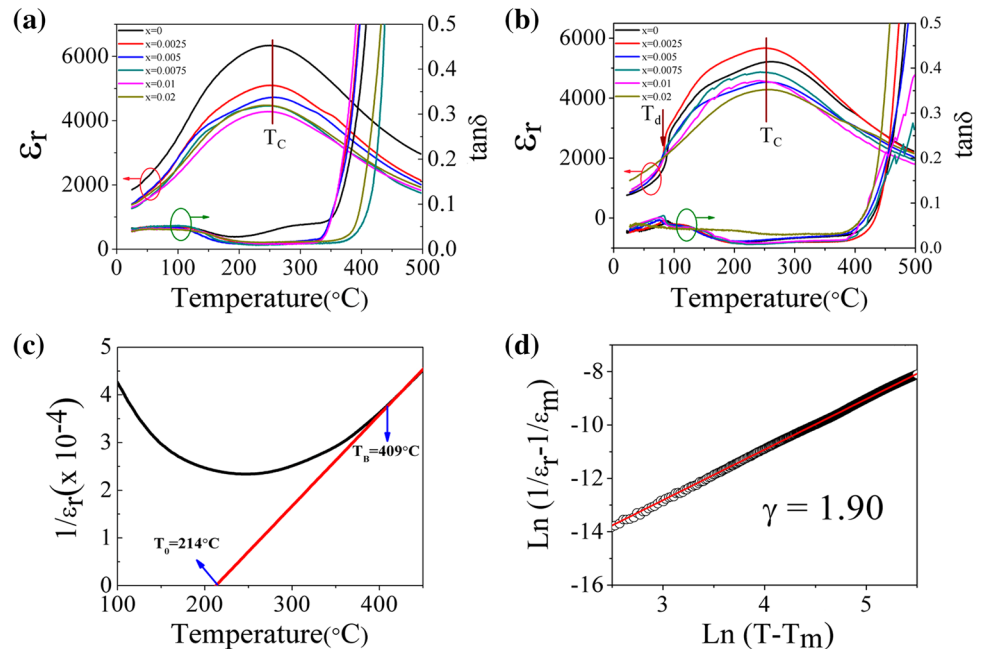


Fig. 3 XRD patterns of the ceramics (a). The magnified view of the peaks corresponding to the maximum intensity (b). Typical result of the Rietveld refinement for the ceramic with $x=0.0025$ (c)

Fig. 4 ϵ_r and $\tan\delta$ of the unpoled ceramics versus temperature at 1 kHz (a). ϵ_r and $\tan\delta$ of the poled ceramics vs. temperature at 1 kHz (b). Plots of the ϵ_r^{-1} versus temperature at 1 kHz for the ceramic with $x=0.01$ (c). Plots of $\ln(1/\epsilon_r - 1/\epsilon_m)$ versus $\ln(T - T_m)$ at 1 kHz for the ceramic with $x=0.01$ (d)



displayed in Table 3. The values of $\Delta T' = T_B - T_C$ reflect the deviation from the CW law. All samples exhibit high $\Delta T'$ values (≥ 100 °C), demonstrating remarkable deviation. The values of $\Delta T = T_C - T_0$ denotes phase transition character, which is positive for first-order phase transition, and zero for second-order phase transition [26]. Here, all ΔT values are larger than zero, indicating the former behavior. The fitting result for the ceramic with $x=0.0025$ according to the modified CW law is shown in Fig. 4d. The modified CW equation is as following:

$$\frac{1}{\epsilon_r} - \frac{1}{\epsilon_m} = \frac{(T - T_c)^\gamma}{C'} \quad (2)$$

where γ and C' are diffusion coefficient and Curie-like constant, respectively [24]. The γ values are always between 1 and 2. Ideal normal ferroelectrics have $\gamma=1$ and ideal relaxor ferroelectrics have $\gamma=2$. All samples have γ values approaching 2 (Table 3), indicating remarkable diffuse behavior. The diffuse character of dielectric behavior in BNT-based ceramics is suggested to be associated with the existence of complex cations, which possess similar radii but different charges and electronic configurations at an equivalent crystallographic site [11, 24, 26].

The polarization (P)–electric field (E) loops of the ceramics measured under various electric fields are shown in Fig. 5. With increasing measurement electric field, hysteresis loops become clear. For the ceramics with high Er^{3+} content, the P–E loops become thinner at a given measurement electric field. The obtained coercive field (E_c), maximum polarization (P_m), and remnant polarization (P_r) at 80 kV/cm are shown in Table 4. For the samples with $x \leq 0.01$, the values of P_m are higher than $40 \mu\text{C}/\text{cm}^2$, P_r values are

Table 2 The values of ϵ_r and $\tan\delta$ at room temperature, ϵ_m , and T_c of the ceramics measured at 1 kHz

Samples	ϵ_r (at R.T.)	$\tan\delta$ (at R.T.)	T_c (°C)	ϵ_m
x=0	1853	0.047	251	6338
x=0.0025	1399	0.042	250	5098
x=0.005	1410	0.043	256	4724
x=0.0075	1269	0.044	245	4461
x=0.01	1308	0.039	247	4280
x=0.02	1384	0.040	243	4476

higher than $30 \mu\text{C}/\text{cm}^2$, and the E_c values are between 35 and 38.2 kV/cm. For the sample with $x=0.02$, both polarization and E_c decrease due to the constriction of the P–E loops. The current density (J)–electric field (E) curves measured at 80 kV/cm are also shown in Fig. 5. For the ceramics with low Er^{3+} doping concentration ($x < 0.01$), two distinct peaks (P_1 and P_2) can be observed on the J–E curves, which is related to the domain switching with changing E [27]. For the ceramic with $x > 0.01$, there appear two other weak peaks (P_3 and P_4), which are related to the transition between ferroelectric order and weak polar phases, as reported by others [28]. The ceramic with $x=0.0025$ exhibits $E_c=36.2$ kV/cm, $P_m=43.7 \mu\text{C}/\text{cm}^2$, and $P_r=34.7 \mu\text{C}/\text{cm}^2$, showing relatively good ferroelectric properties. The d_{33} values are also shown in Table 4. The ceramics with $x \leq 0.0075$ exhibit high d_{33} values between 132 and 137 pC/N. As x increases to 0.02, the d_{33} of the ceramic decreases to 61 pC/N. The piezoelectric constant and polarization have the relationship of $d_{33} \propto \epsilon_{33} \epsilon_0 Q P_r$, where ϵ_0 is vacuum permittivity, Q is electrostrictive coefficient, ϵ_{33} is intrinsic dielectric permittivity in the direction of the polarization [29]. Generally, high polarization corresponds to high piezoelectric constant. The low polarization of the ceramic with $x=0.02$ should be responsible for its low d_{33} .

Fluorescence emission spectra of the ceramics under the excitation of 487 nm are shown in Fig. 6a. All ceramics exhibit two luminescent emission bands around 650–675 nm (red light) and 520–560 nm (green light). Figure 6b shows the schematic energy level of Er^{3+} . Electrons in ground state $^4I_{15/2}$ can jump to $^4F_{5/2}$ and $^4F_{7/2}$ under the excitation of 450 nm and 487 nm, respectively. Energy radiative

relaxation of the electrons in these two states can happen to the mixed energy ($^2H_{11/2}$, $^4S_{3/2}$, $^4F_{9/2}$) under the action of multi-phonon radiation. In this case, red (528 nm, 549 nm) and green (670 nm) light can be observed under excitation at 450 and 487 nm, respectively. The radiative relaxation down to $^2H_{11/2}$, $^4S_{3/2}$, $^4F_{9/2}$ and the followed transition to the ground state cause the emission of red (528, 549 nm) and green (670 nm) light. But, the transits of $^4F_{7/2} + ^4I_{11/2} \rightarrow ^4F_{9/2}$ and $^4H_{11/2} + ^4I_{15/2} \rightarrow ^4F_{9/2} + ^4I_{13/2}$ result in reduction of electrons in $^4F_{7/2}$ and $^2H_{11/2}$. The green emission has two obvious strong peaks, corresponding to the wavelength of 528 nm and 548 nm, which are attributed to the transitions of $^2H_{11/2} \rightarrow ^4I_{15/2}$ and $^4S_{3/2} \rightarrow ^4I_{15/2}$, respectively. The red emission (670 nm) is attributed to the transition of $^4F_{9/2} \rightarrow ^4I_{15/2}$. The inset displays the emission intensity of the ceramics with the different Er^{3+} amounts. The intensity of green emission increases first as x is between 0 and 0.0075, and then decreases with further increasing x . The intensity of red emission increases continuously with increasing x . With the increase in the Er^{3+} concentration, the absorbing pumping source increases, and thus the intensity of emission spectra of different bands increases. But, in the case of higher Er^{3+} doping concentration, the distance between neighboring Er^{3+} ions should shorten. The complex crossover relaxation and energy transfer processes become more efficient, which enhances quenching of the green emission and thus weakens the green emission [30, 31]. However, such processes cause more electrons at $^4F_{9/2}$ level, and then induce more transitions from $^4F_{9/2}$ to $^4I_{15/2}$, which increases red intensity [17, 31].

4 Conclusions

The $(\text{Bi}_{0.5-x}/0.94\text{Er}_{x/0.94}\text{Na}_{0.5})_{0.94}\text{Ba}_{0.06}\text{TiO}_3$ lead-free ceramics with high density were successfully obtained. All samples have pure phase and average grain sizes between 0.6 and 1.0 μm . The Curie temperature of the ceramics are between 243 and 256 °C. The ceramic with $x=0.0025$ exhibits E_c of 36.2 kV/cm, P_m of 43.7 $\mu\text{C}/\text{cm}^2$, P_r of 34.7 $\mu\text{C}/\text{cm}^2$, and d_{33} of 137 pC/N. The green emission on luminescent emission spectrum shows two distinct peaks at 528 nm and 548 nm. The ceramic with $x=0.0075$

Table 3 The fitting values via the Curie–Weiss law and modified Curie–Weiss law

Samples	T_0 (°C)	T_B (°C)	T_c (°C)	$\Delta T' = T_B - T_c$	$\Delta T = T_c - T_0$	γ
x=0	188	403	251	152	63	1.79
x=0.0025	233	405	250	155	17	1.82
x=0.005	218	404	256	148	38	1.83
x=0.0075	136	345	245	100	109	1.97
x=0.01	214	409	247	162	33	1.90
x=0.02	214	409	243	166	29	1.96

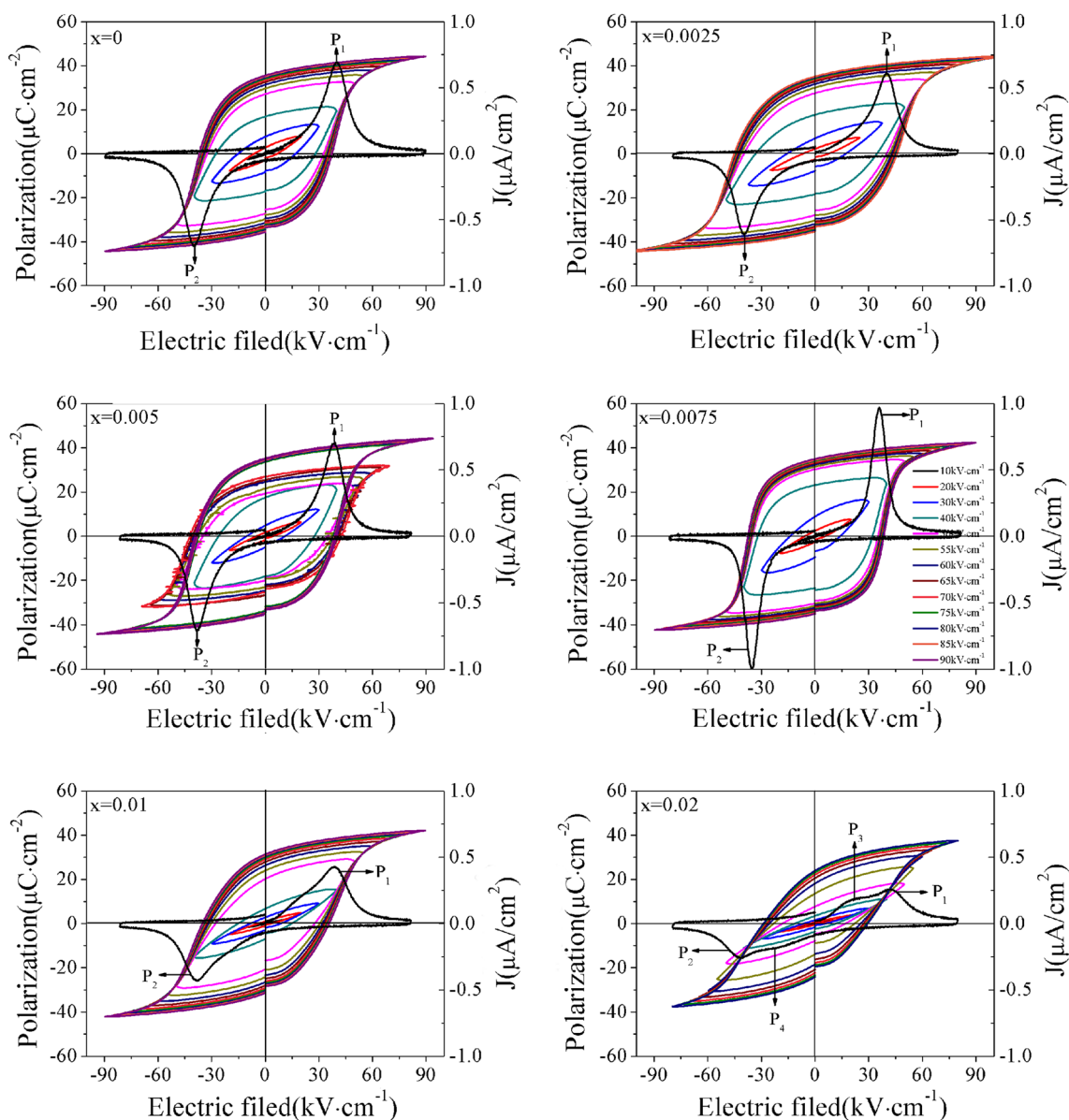


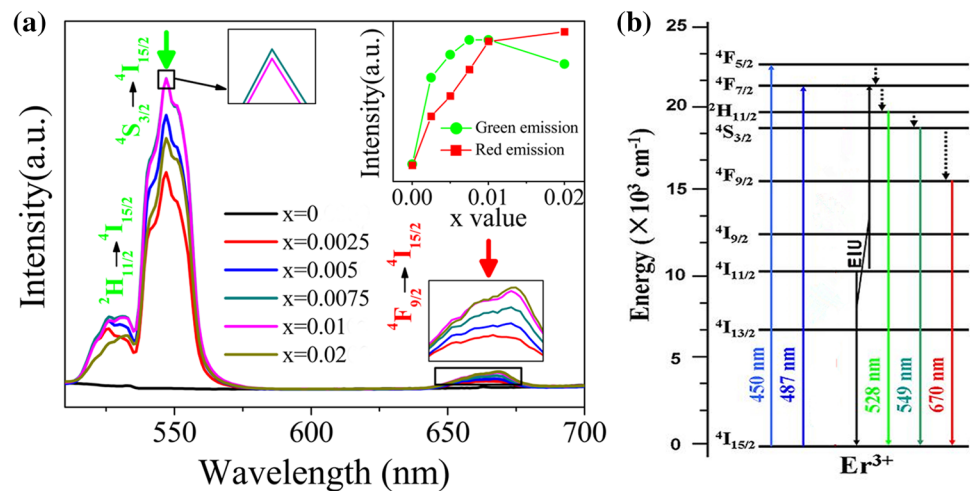
Fig. 5 P–E and J–E loops of the ceramics measured at room temperature

Table 4 The values of remnant polarization (P_r), maximum polarization (P_m), and coercive field (E_c) measured at 80 kV/cm and d_{33} values of the ceramics

Samples	E_c (kV/cm)	P_m ($\mu\text{C}/\text{cm}^2$)	P_r ($\mu\text{C}/\text{cm}^2$)	d_{33} (pC/N)
x=0	38.0	42.8	34.3	132
x=0.0025	36.2	43.7	34.7	137
x=0.005	38.2	42.3	34.1	136
x=0.0075	36.8	41.1	34.7	135
x=0.01	35.0	40.6	30.4	121
x=0.02	29.4	37.5	24	61

exhibits the maximum intensity of green emission. The red emission between 650 and 675 nm shows an obvious peak corresponding to the transition from ${}^4\text{F}_{9/2}$ to ${}^4\text{I}_{15/2}$. With increasing x, the intensity of red emission increases continuously.

Fig. 6 Photoluminescence spectra of the ceramics under the excitation of 487 nm **(a)**. The insets show the composition-dependent green and red emission intensities and enlarged local patterns. Schematic energy level of Er^{3+} **(b)**



Acknowledgements This work was supported by Shaanxi Province Science and Technology Foundation (2018JM1009), Fundamental Research Funds for the Central Universities (Nos. GK201803017, GK201901005), and National Innovation and Entrepreneurship Training Program for College Students (No. CX2018105).

References

- G.H. Haertling, *J. Am. Ceram. Soc.* **82**, 797 (1999)
- L.J. Liu, M. Knapp, H. Ehrenberg, L. Fang, L.A. Schmitt, H. Fuess, M. Hoelzel, M. Hinterstein, *J. Appl. Crystallogr.* **49**, 574 (2016)
- D.W. Wang, F. Hussain, A. Khesro, A. Feteira, Y. Tian, Q.L. Zhao, I.M. Reaney, *J. Am. Ceram. Soc.* **100**, 627 (2017)
- C. Pascual-Gonzalez, G. Schileo, S. Murakami, A. Khesro, D.W. Wang, *Appl. Phys. Lett.* **110**, 172902 (2017)
- C. Pascual-Gonzalez, G. Schileo, A. Khesro, I. Sterianou, D.W. Wang, I.M. Reaney, A. Feteira, *J. Mater. Chem. C* **5**, 1990 (2017)
- S.Z. Erika Odendo, L.J. Liu, D.P. Shi, Y.M. Huang, L.L. Fan, J. Chen, L. Fang, B. Elouadi, *J. Appl. Phys.* **113**, 094102 (2013)
- T. Takenaka, K. Maruyama, K. Sakata, *J. Appl. Phys.* **30**, 2236 (1991)
- L.J. Liu, D.P. Shi, M. Knapp, H. Ehrenberg, L. Fang, J. Chen, *J. Appl. Phys.* **116**, 184104 (2014)
- F. Li, G.R. Chen, X. Liu, J.W. Zhai, B. Shen, S.D. Li, P. Li, K. Yang, H.R. Zeng, H.X. Yan, *Appl. Phys. Lett.* **110**, 182904 (2017)
- X.S. Qiao, X.M. Chen, H.L. Lian, J.P. Zhou, P. Liu, *J. Eur. Ceram. Soc.* **36**, 3995 (2016)
- X.S. Qiao, X.M. Chen, H.L. Lian, W.T. Chen, J.P. Zhou, P. Liu, *J. Am. Ceram. Soc.* **99**, 198 (2016)
- J. Glaum, H. Simons, M. Acosta, M. Hoffman, *J. Am. Ceram. Soc.* **96**, 2881 (2013)
- H.Q. Sun, D.F. Peng, X.S. Wang, M.M. Tang, Q.W. Zhang, X. Yao, *J. Appl. Phys.* **110**, 016102 (2011)
- H.L. Pan, J.J. Zhang, X.R. Jia, H.J. Xing, J.Y. He, J.Y. Wang, F. Wen, *Ceram. Int.* **44**, 5785 (2018)
- A.S. Herabut, *J. Am. Ceram. Soc.* **80**, 2954 (1997)
- H.Q. Sun, Q.W. Zhang, X.S. Wang, Y. Zhang, *Ceram. Int.* **40**, 15669 (2014)
- B. Hu, Z. Pan, M. Dai, F.F. Guo, H.P. Ning, Z.B. Gu, J. Chen, M.H. Lu, S.T. Zhang, B. Yang, W.W. Cao, *J. Am. Ceram. Soc.* **97**, 3877 (2014)
- C.M. Lau, X. Wu, K.W. Kwok, *J. Appl. Phys.* **118**, 034107 (2015)
- B.H. Toby, *J. Appl. Cryst.* **34**, 210 (2001)
- D.W. Wang, Z.M. Fan, D. Zhou, A. Khesro, S. Murakami, A. Feteira, Q.L. Zhao, X.L. Tan, I.M. Reaney, *J. Mater. Chem. A* **6**, 4133 (2018)
- D.W. Wang, Z.M. Fan, W.B. Li, D. Zhou, A. Feteira, G. Wang, S. Murakami, S. Sun, Q.L. Zhao, X.L. Tan, I.M. Reaney, *ACS Appl. Energy Mater.* **1**, 4403 (2018)
- R.D. Shannon, *Acta Crystallogr. A* **32**, 751 (1976)
- C.W. Tai, S.H. Choy, H.L.W. Chan, *J. Am. Ceram. Soc.* **91**, 3335 (2008)
- R.Y. Jing, X.M. Chen, H.L. Lian, X.S. Qiao, X.J. Shao, J.P. Zhou, *J. Eur. Ceram. Soc.* **38**, 3111 (2018)
- T. Wang, X.M. Chen, Y.Z. Qiu, H.L. Lian, W.T. Chen, *Mater. Chem. Phys.* **186**, 407 (2017)
- Z.D. Yu, X.M. Chen, *Physica B* **503**, 7 (2016)
- L. Jin, F. Li, S. Zhang, *J. Am. Ceram. Soc.* **97**, 1 (2014)
- G. Dong, H. Fan, J. Shi et al., *J. Am. Ceram. Soc.* **98**, 1150 (2015)
- Q.M. Zhang, H. Wang, N. Kim, L.E. Cross, *J. Appl. Phys.* **75**, 454 (1994)
- D.F. Peng, X.S. Wang, C.N. Xu, X. Yao, J. Lin, T.T. Sun, *J. Am. Ceram. Soc.* **96**, 184 (2013)
- S. Chen, M.J. Wu, L.Q. An, Y.X. Li, S.W. Wang, *J. Am. Ceram. Soc.* **90**, 664 (2007)

Publisher's Note Springer Nature remains neutral with regard to jurisdictional claims in published maps and institutional affiliations.